Bulletin of the Seismological Society of America, Vol. 82, No. 4, pp. 1927–1955, August 1992

WAVE FIELDS FROM AN OFF-CENTER EXPLOSION IN AN EMBEDDED SOLID SPHERE

By Lian-She Zhao and David G. Harkrider

Abstract

This study investigates the effects of explosions in asymmetric source regions on the excitation of seismic body waves. We give an analytic formulation for determining the wave fields from an off-center explosion in an embedded solid sphere in an elastic whole-space. As expected, this geometry generates shear as well as compressional body waves. The calculated wave fields show that the degree of shear-wave generation is determined by the asymmetry of the source region. The results are compared with the known analytic solutions of an explosion in an elastic whole-space and at the center of an elastic sphere embedded in the whole-space. The radiation patterns at different periods for different parameters of the media suggest that the asymmetry of the source region has significant effects on shorter period but has only minor effects on long periods. The long-period *P*-to-*S* wave maximum amplitude results are in agreement with that for explosions in axisymmetric cavities.

Introduction

Shear waves are almost always observed from underground explosions. One can visualize many ways to convert explosion P waves into SV waves. An obvious mechanism is the free-surface or other nearby planar boundaries. But the presence of SH waves is especially perplexing. The SH waves are generally considered to be due to tectonic release from the volume relaxation of the local prestress surrounding the shot point or as a triggered earthquake on nearby fault planes (Aki and Tsai, 1972; Press and Archambeau, 1962). Other mechanisms for SH-wave excitation have also been investigated, such as the conversion of source P waves from explosions in long narrow valleys and the generation of S waves by explosions in anisotropic media and axisymmetric cavities (Ben-Menahem and Sena, 1990; Glenn *et al.*, 1985, 1986; Mandal and Toksöz, 1990; and Rial and Moran, 1986).

We show in this paper that a significant amount of shear waves can be generated by an asymmetric source region. We give the formulation for the wave fields of an off-center explosive source in an elastic homogeneous sphere embedded in an elastic homogeneous whole-space with different elastic constants and densities. Ours differs from the usual scattering due to spherical inclusions problem found in the acoustic literature. For instance, Pao (1978) gives the scattering or transition matrix (Varatharajulu and Pao, 1976; Waterman, 1969, 1976) solution for a spherical cavity, a rigid sphere in a solid, and an elastic sphere in a fluid and a solid. The scattering matrix formulation is then compared to earlier obtained solutions for an incident plane wave with a stationary or sinusoidal time history (Pao and Mow, 1973). The effect of restricting the source duration to be finite for an incident plane P wave on a solid sphere is considered by Dubrovskiy and Morochnik (1989). The solution due to a spherical incident wave is given in Pao and Mow (1973). The only solution found by the authors for a source embedded eccentrically within a sphere was that by

Thompson (1973) for a spherical source embedded in a fluid sphere in a fluid space. That problem is the fluid or acoustical analog to our problem.

As in Thompson (1973), we expand the wave fields in spherical harmonics and use the interface boundary conditions at the spherical contact, welded in this case, to find the coefficient of the expansion. Since this is a whole-space problem, the separation of the shear displacement field into *SV* and *SH* waves and potentials may seem an unwarranted complication. But, for completeness and for use in a later paper, we present potential expressions in Appendix A for an arbitrary orientation of the symmetry axis, which will facilitate the incorporation of this source into a vertically inhomogeneous elastic half-space problem. Initially, for ease of formulation, the spherical coordinate system is oriented with the source on the vertical axis, i.e., $\theta = 0$, so that only *SV* waves are generated. Once the displacement field is obtained, the coordiante system is rotated for a more general source orientation and expressions are then given in Appendix A to convert the wave fields into *P*-, *SV*-, and *SH*-wave potentials and their respective displacement fields.

Theory

The geometry and the coordiante system are given in Figure 1. The displacement resulting from an explosive source located at the spherical coordinates, (r_0, θ_0, ϕ_0), in a homogeneous, isotropic, unbounded elastic medium may be expressed in the form (Ben-Menahem and Singh, 1981, p. 384):

$$\mathbf{u}_0 = ik_\alpha g(\omega) A_0 \nabla h_0^{(2)}(k_\alpha R),$$

where the receiver is located at (r, θ, ϕ); $g(\omega)$ is the spectrum of explosive source function; ∇ is gradient; $h_0^{(2)}(k_\alpha R)$ is spherical Hankel function of second kind; $k_\alpha = \omega/\alpha$; α is the compressional velocity; $\alpha^2 = (\lambda + 2\mu)/\rho$ in terms of the density ρ and the lame' constants λ and μ; R is distance between source and receiver; and

$$A_0 = \frac{M_0}{4\pi(\lambda + 2\mu)},$$

where M_0 is the seismic moment.

We now express the spherical Hankel function $h_0^{(2)}(k_\alpha R)$ in terms of r_0, r, and the angle δ between the position vectors of the source and receiver as

$$h_0^{(2)}(k_\alpha R) = \sum_{l=0}^{l=\infty} (2l + 1) j_l(k_\alpha r_0) h_l^{(2)}(k_\alpha r) P_l(\cos \delta),$$

where $r \geqq r_0$, $j_l(k_\alpha r)$ is the spherical Bessel function; and $P_l(\cos \theta)$ is the Legendre function. Initially we replace δ by θ. This is equivalent to assuming that the source is located on the z axis, that is, $\theta_0 = 0$. With this substitution, the displacement expression becomes

$$\mathbf{u}_0 = ik_\alpha^2 g(\omega) A_0 \sum_{l=0}^{l=\infty} (2l + 1) j_l(k_\alpha r_0) \mathbf{L}_{0l}^-(k_\alpha r)$$

for $r \geqq r_0$ and where $\mathbf{L}_{0l}^-(k_\alpha r)$ is defined below.

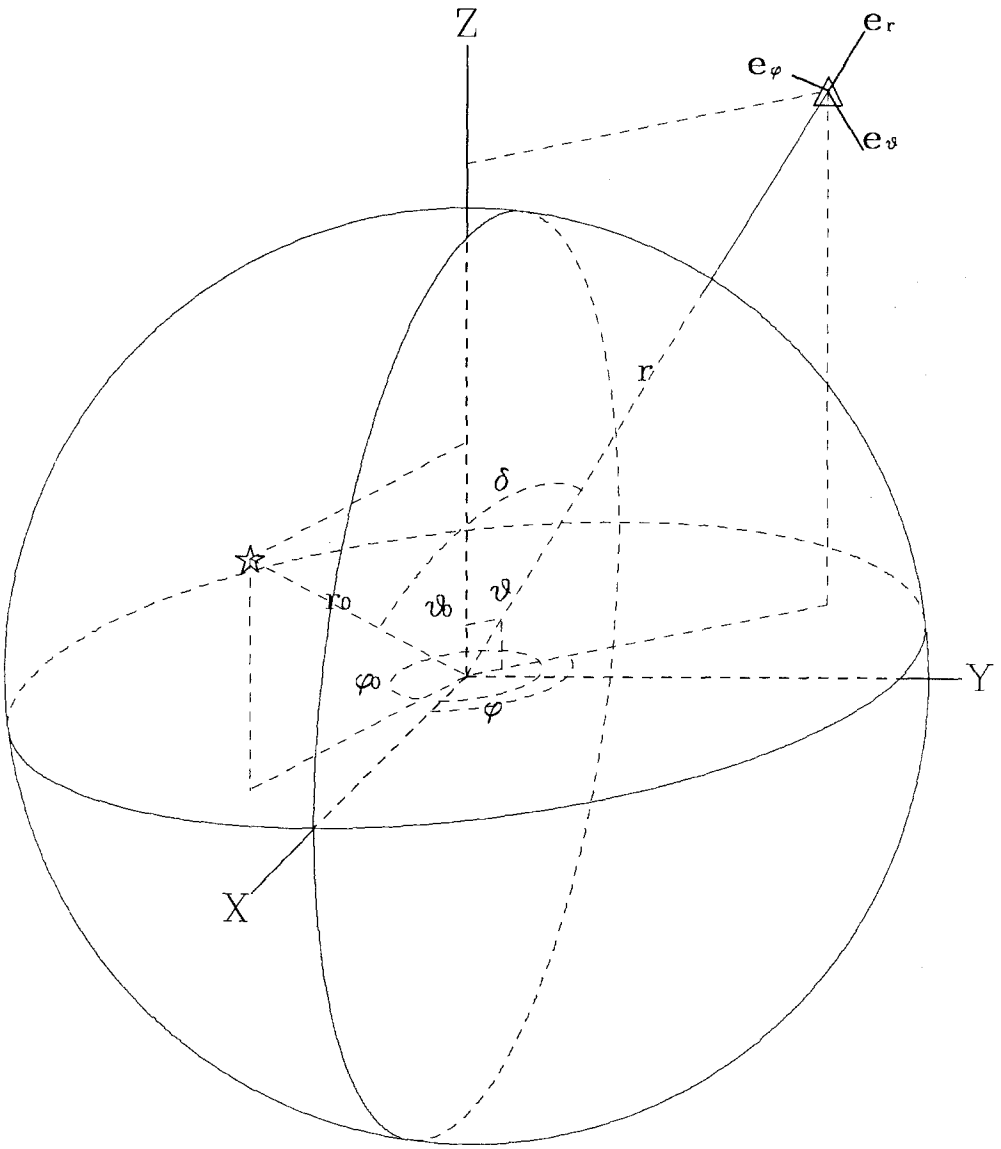

FIG. 1. The geometry and the coordinate system used in this study. Star is source, and triangle is receiver.

If we bound the source medium by a sphere of radius $r = a$, we can assume the displacement field inside and outside as

$$\mathbf{u}_1 = \mathbf{u}_0 - \sum_{l=0}^{l=\infty} (2l+1)\left[a_l \mathbf{N}_{0l}^{+}(k_{\beta_1} r) + b_l \mathbf{L}_{0l}^{+}(k_{\alpha_1} r)\right] \tag{1a}$$

for $r > r_0$, $r \leqq a$ and

$$\mathbf{u}_2 = \sum_{l=0}^{l=\infty} (2l+1)\left[c_l \mathbf{N}_{0l}^{-}(k_{\beta_2} r) + d_l \mathbf{L}_{0l}^{-}(k_{\alpha_2} r)\right] \tag{1b}$$

for $r \geq a$, where $k_\beta = \omega/\beta$; β is the shear velocity; and $\beta^2 = \mu/\rho$. The boundary conditions to be satisfied at $r = a$ are

$$\mathbf{u}_1 = \mathbf{u}_2, \tag{2a}$$

$$\mathbf{e}_r \cdot \boldsymbol{\Xi}(\mathbf{u}_1) = \mathbf{e}_r \cdot \boldsymbol{\Xi}(\mathbf{u}_2), \tag{2b}$$

where $\boldsymbol{\Xi}$ is the stress dyadic. The displacement and stress dyadic can be conveniently expressed in terms of the Hansen vectors, which are the eigenvector solutions of the force-free Navier equation (Ben-Menahem and Singh, 1981, Chapter 2). The Hansen vectors in terms of spherical harmonics are

$$\mathbf{L}^{\pm}_{ml}(\xi) = \frac{d}{d\xi} f_l^{\pm}(\xi)\mathbf{P}_{ml}(\theta, \phi) + \frac{1}{\xi} f_l^{\pm}(\xi)[l(l+1)]^{1/2}\mathbf{B}_{ml}(\theta, \phi),$$

$$\mathbf{N}^{\pm}_{ml}(\eta) = \frac{1}{\eta} f_l^{\pm}(\eta) l(l+1)\mathbf{P}_{ml}(\theta, \phi) + \left(\frac{d}{d\eta} + \frac{1}{\eta}\right) f_l^{\pm}(\eta)[l(l+1)]^{1/2}\mathbf{B}_{ml}(\theta, \phi),$$

where

$$\mathbf{P}_{ml}(\theta, \phi) = \mathbf{e}_r P_l^m(\cos\theta) e^{im\phi} = \mathbf{e}_r Y_{ml}(\theta, \phi),$$

$$\sqrt{l(l+1)}\,\mathbf{B}_{ml} = \left(\mathbf{e}_\theta \frac{\partial}{\partial\theta} + e_\phi \frac{\partial}{\sin\theta\,\partial\phi}\right) P_l^m(\cos\theta) e^{im\phi},$$

and where $\xi = k_\alpha r$, $\eta = k_\beta r$, $f_l^{+}(z) = j_l(z)$, and $f_l^{-}(z) = h_l^{(2)}(z)$.

The corresponding stresses are given by

$$\mathbf{e}_r \cdot \boldsymbol{\Xi}(\mathbf{L}) = 2\mu k_\alpha \left[F_{l,3}(\xi)\mathbf{P}_{ml} + F_{l,1}(\xi)[l(l+1)]^{1/2}\mathbf{B}_{ml}\right],$$

$$\mathbf{e}_r \cdot \boldsymbol{\Xi}(\mathbf{N}) = \mu k_\beta \left[2l(l+1)F_{l,1}(\eta)\mathbf{P}_{ml} + F_{l,2}(\eta)[l(l+1)]^{1/2}\mathbf{B}_{ml}\right].$$

The functions $\mathbf{F}_{l,i}$ are given by

$$F^{\pm}_{l,1}(z) = \frac{1}{z}\left(\frac{d}{dz} - \frac{1}{z}\right) f_l^{\pm}(z) = \frac{(l-1)}{z^2} f_l^{\pm}(z) - \frac{1}{z} f^{\pm}_{l+1}(z),$$

$$F^{\pm}_{l,2}(z) = \left[\frac{2}{z^2}(l^2-1) - 1\right] f_l^{\pm}(z) + \frac{2}{z} f^{\pm}_{l+1}(z) = \frac{d_2 f_l^{\pm}}{dz^2} + \frac{(l-1)(l+2)}{z^2} f_l^{\pm}(z),$$

$$F^{\pm}_{l,3}(z) = \left[\frac{1}{z^2} l(l-1) - \frac{1}{2}\left(\frac{\alpha}{\beta}\right)^2\right] f_l^{\pm}(z) + \frac{2}{z} f^{\pm}_{l+1}(z) = \frac{d^2}{dz^2} f_l^{\pm} - \frac{\lambda}{2\mu} f_l^{\pm}(z).$$

Substituting the above into equation (1), we have for the lth components of the displacements

$$\begin{aligned}\mathbf{u}_{1l} = {} & ik_{\alpha_1}^2 g(\omega) A_0 (2l+1) j(k_{\alpha_1} r_0) \left[f_l^{-\prime}(\xi_1) P_l \mathbf{e}_r + \frac{1}{\xi_1} f_l^{-}(\xi_1) \frac{d}{d\theta} P_l \mathbf{e}_\theta \right] \\ & - (2l+1) a_l \frac{N^2}{\eta_1} f_l^{+}(\eta_1) P_l \mathbf{e}_r - (2l+1) a_l \left(\frac{d}{d\eta} + \frac{1}{\eta_1} \right) f_l^{+}(\eta_1) \frac{d}{d\theta} P_l \mathbf{e}_\theta \\ & - (2l+1) b_l f_l^{+\prime}(\xi_1) P_l \mathbf{e}_r - (2l+1) b_l f_l^{+}(\xi_1) \frac{1}{\xi_1} \frac{d}{d\theta} P_l \mathbf{e}_\theta, \qquad (3)\end{aligned}$$

$$\begin{aligned}\mathbf{u}_{2l} = {} & (2l+1) c_l \frac{N^2}{\eta_2} f_l^{-}(\eta_2) P_l \mathbf{e}_r + (2l+1) c_l \left(\frac{d}{d\eta} + \frac{1}{\eta_2} \right) f_l^{-}(\eta_2) \frac{d}{d\theta} P_l \mathbf{e}_\theta \\ & + (2l+1) d_l f_l^{-\prime}(\xi_2) P_l \mathbf{e}_r + (2l+1) d_l f_l^{-}(\xi_2) \frac{1}{\xi_2} \frac{d}{d\theta} P_l \mathbf{e}_\theta,\end{aligned}$$

and the lth components of the spherical surface tractions

$$\begin{aligned}\mathbf{e}_r \cdot \Xi(\mathbf{u}_{1l}) = {} & ik_{\alpha_1}^2 g(\omega) A_0 (2l+1) j_l(k_{\alpha_1} r_0) \\ & \cdot \left[F_{l,3}^{-}(\xi_1) P_l(\cos\theta) \mathbf{e}_r + F_{l,1}^{-}(\xi_1) \frac{d}{d\theta} P_l(\cos\theta) \mathbf{e}_\theta \right] \\ & - (2l+1) a_l \mu_1 k_{\beta_1} \\ & \cdot \left[2N^2 F_{l,1}^{+}(\eta_1) P_l(\cos\theta) \mathbf{e}_r + F_{l,2}^{+}(\eta_1) \frac{d}{d\theta} P_l(\cos\theta) \mathbf{e}_\theta \right] \\ & - 2(2l+1) b_l \mu_1 k_{\alpha_1} \\ & \cdot \left[F_{l,3}^{+}(\xi_1) P_l(\cos\theta) \mathbf{e}_r + F_{l,1}^{+}(\xi_1) \frac{d}{d\theta} P_l(\cos\theta) \mathbf{e}_\theta \right]\end{aligned}$$

$$\begin{aligned}\mathbf{e}_r \cdot \Xi(\mathbf{u}_{2l}) = {} & (2l+1) c_l \mu_2 k_{\beta_2} \left[2N^2 F_{l,1}^{-}(\eta_2) P_l(\cos\theta) \mathbf{e}_r + F_{l,2}^{-}(\eta_2) \frac{d}{d\theta} P_l(\cos\theta) \mathbf{e}_\theta \right] \\ & + 2(2l+1) d_l \mu_2 k_{\alpha_2} \\ & \cdot \left[F_{l,3}^{-}(\xi_2) P_l(\cos\theta) \mathbf{e}_r + \mathbf{F}_{l,1}^{-}(\xi_2) \frac{d}{d\theta} P_l(\cos\theta) \mathbf{e}_\theta \right],\end{aligned}$$

where $N^2 = l(l+1)$ and the prime ($'$) denotes differentiation by the functions argument, and where $\xi_1 = k_{\alpha_1} a$, $\eta_1 = k_{\beta_1} a$, $\xi_2 = k_{\alpha_2} a$, and $\eta_2 = k_{\beta_2} a$.

Using equations (2), and comparing the coefficients of $P_l(\cos\theta)\mathbf{e}_r \cdot \mathbf{u}_l$, $(dP_l(\cos\theta)/d\theta)\mathbf{e}_\theta \cdot \mathbf{u}_l$, $P_l(\cos\theta)\mathbf{e}_r \cdot \Xi(\mathbf{u}_l) \cdot \mathbf{e}_r$, and $(dP_l(\cos\theta)/d\theta)\mathbf{e}_r \cdot \Xi(\mathbf{u}_l) \cdot \mathbf{e}_\theta$, we have the matrix equation

$$YC = D, \qquad (4)$$

where

$$D = ik_{\alpha_1}^2 g(\omega) A_0 j_l(k_{\alpha_1} r_0) \left[f_l^{-\prime}(\xi_1), \frac{1}{\xi_1} f_l^{-}(\xi_1), 2\mu_1 k_{\alpha_1} F_{l,3}^{-}(\xi_1), 2\mu_1 k_{\alpha_1} F_{l,1}(\xi_1) \right]^T, \tag{5}$$

$$C = (a_l, b_l, c_l, d_l)^T, \tag{6}$$

$$\mathbf{Y} = \begin{bmatrix} \frac{N^2}{\eta_1} f_l^{+}(\eta_1) & f_l^{+\prime}(\xi_1) & \frac{N^2}{\eta_2} f_l^{-}(\eta_2) & f_l^{-\prime}(\xi_2) \\ \left(\frac{d}{d\eta} + \frac{1}{\eta_1}\right) f_l^{+}(\eta_1) & \frac{1}{\xi_1} f_l^{+}(\xi_1) & \left(\frac{d}{d\eta} + \frac{1}{\eta_2}\right) f_l^{-}(\eta_2) & \frac{1}{\xi_2} f_l^{-}(\xi_2) \\ 2\mu_1 k_{\beta_1} N^2 F_{l,1}^{+}(\eta_1) & 2\mu_1 k_{\alpha_1} F_{l,3}^{+}(\xi_1) & 2\mu_2 k_{\beta_2} N^2 F_{l,1}^{-}(\eta_2) & 2\mu_2 k_{\alpha_2} F_{l,3}^{-}(\xi_2) \\ \mu_1 k_{\beta_1} F_{l,2}^{+}(\eta_1) & 2\mu_1 k_{\alpha_1} F_{l,1}^{+}(\xi_1) & \mu_2 k_{\beta_2} F_{l,2}^{-}(\eta_2) & 2\mu_2 k_{\alpha_2} F_{l,1}^{-}(\xi_2) \end{bmatrix}, \tag{7}$$

where T denotes transpose. We can now determine the coefficients (6) of the expansion (1) and equation (3) by equation (4).

Even though the potential relations in Appendix A are convenient for including this source in propagator and generalized ray calculations, they are awkward for evaluating the whole space wave fields. For this, we introduce an alternative approach. If the source is located at $(r_0, 0, 0)$, the displacement fields are given by equations (1). Generally, if the source is located at (r_0, θ_0, ϕ_0), Figure 1, θ and ϕ should be changed to δ and γ, with $\cos\delta = \cos\theta\cos\theta_0 + \sin\theta\sin\theta_0\cos(\phi - \phi_0)$. The range of δ is 0 to 360°, and δ is defined as the angle measured clockwise from the position vector of the source to the position vector of the receiver. For this source geometry, the coordiante system with $\mathbf{e}_{r_0}$ as the north pole has unit base vectors $(\mathbf{e}_r, \mathbf{e}_\delta, \mathbf{e}_\gamma)$, and coordinates (r, δ, γ). Even though there are no displacements in the γ direction for this symmetry, the most straightforward way of defining δ is in terms of $\mathbf{e}_\gamma$, the normal to the plane containing r_0 and r. The displacement fields are now written as

$$\mathbf{u} = (u_P{}^r + u_{SV}^r)\mathbf{e}_r + (u_P{}^\delta + u_{SV}^\delta)\mathbf{e}_\delta, \tag{8}$$

where

$$\begin{aligned} \mathbf{e}_\delta &= \mathbf{e}_\gamma \times \mathbf{e}_r \\ &= \frac{1}{\sin\delta}(\mathbf{e}_r(\mathbf{e}_r \cdot \mathbf{e}_{r_0}) - \mathbf{e}_{r_0}), \end{aligned}$$

since

$$\mathbf{e}_\gamma = \mathbf{e}_{r_0} \times \mathbf{e}_r / \sin\delta.$$

The P and SV displacements, u^r and u^δ, are obtained by summing over l the coefficients of $\mathbf{e}_r$ and $\mathbf{e}_\delta$ in the second of equations (3). Resolving the angular displacements, u^δ into the more general coordinate system (r, θ, ϕ), we can

write the displacement fields as

$$\mathbf{u} = u^r \mathbf{e}_r + u^\theta \mathbf{e}_\theta + u^\phi \mathbf{e}_\phi, \tag{9}$$

with

$$u^r = u_P{}^\delta + u_{SV}^r,$$

$$u^\theta = -\left(u_P{}^\delta + u_{SV}^\delta\right)(\sin\theta_0 \cos\theta \cos(\phi - \phi_0) - \cos\theta_0 \sin\theta)/\sin\delta,$$

and

$$u^\phi = \left(u_P{}^\delta + u_{SV}^\delta\right)\sin\theta_0 \sin(\phi - \phi_0)/\sin\delta.$$

When $\delta = 0$ *or* 180°, equations (9) no longer hold. This is when the source and receiver are on a line through the sphere origin and then we should use equations (3).

Before going on to numerical examples, there is one further point to discuss: the inferred seismic moment. In the following, we assume that the observed seismic radiation can be inverted back to the source region using appropriate Green's functions. We further assume that the observers either do not know the details of the source's environment, such as in this case the material properties of the embedded sphere, or if they do have this knowledge, they decide not to correct for it. Then, the source region properties used in the Green's functions are that of the exterior medium, and we will refer to this inverted moment as the inferred or "observed" seismic moment. For our source, the "observed" seismic moment is

$$M_{obs} = \frac{\rho_2 \alpha_2{}^2}{\rho_1 \alpha_1{}^2 + {}^4/_3\left(\rho_2 \beta_2{}^2 - \rho_1 \beta_1{}^2\right)} M_0, \tag{10}$$

where M_0 is the input moment of the explosion. By input moment, we mean the moment that would be measured if the confining or shot point medium of the sphere was a whole-space. This equation is obtained by using equation (B4) of Appendix B and letting ω go to zero. Since nuclear explosion sources are frequently characterized by A_0 or the more familiar notation, $\Psi(\infty)$, which is the asymptotic value of the reduced displacement potential for large time, and

$$M_0 = 4\pi\rho\alpha^2\Psi(\infty),$$

we can write equation (10) as

$$\Psi(\infty)_{obs} = \frac{1}{1 + \frac{4}{3}\frac{\beta_1{}^2}{\alpha_1{}^2}\left(\frac{\mu_2}{\mu_1} - 1\right)}\Psi(\infty), \tag{11}$$

where the elastic rigidity $\mu = \rho\beta^2$ and as before the subscript 1 denotes the inclusion or shot point material and 2 denotes the exterior medium. Thus, the difference between "observed" and shot point $\Psi(\infty)$ is independent of density contrast and in source media with similar Poisson ratios is only a function of the

rigidity ratio of the material in which the $\Psi(\infty)$ is measured and the shot point material. The smaller the shot point rigidity, the smaller the "observed" $\Psi(\infty)$ while large shot point rigidities cause amplification. Since the minimum realistic ratio of P-to-S wave ratios is $\sqrt{2}$, which corresponds to a Poisson ratio of zero, the maximum possible amplification is a factor of 3.

RESULTS

In this section, we present some numerical results. For all of the synthetics, we assume that the moment time history is a step function, i.e.,

$$g(\omega) = 1/i\omega,$$

and

$$M_0 = 4\pi\rho_1\alpha_1^2 \times 10^{20} \text{ dyne-cm},$$

where ρ is in g/cm^3, and the velocities, α and β, are in km/sec, and distances in km. Thus $\Psi(\infty)$ is kept the same for the different spherical source media models. The distances are in km and the displacement is in cm. The spectral band-width is from 102.4 sec in period to 10 Hz. As our standard model, we assume the elastic parameters and dimensions given in Table 1. The receiver is located 10 km from the center of the elastic sphere unless otherwise indicated. The material model for the whole-space outside of the sphere is reasonable for sedimentary regions; see for example Zhao *et al.* (1991). When investigating the effect of different elastic properties of the sphere, Nafe's velocity-density relation (Ludwig *et al.*, 1970) is used to obtain densities and S-wave velocities for a given P velocity. We used 20 terms to sum up the wave fields; see equation (1). The error induced from truncation of order m is approximately the order $m^6(r_0/r)^m$. This error determination is from the eccentricity expansion or addition theorem of equation (1) and depends on the ratio of the arguments of the Bessel and Hankel functions used in the series expansion, which in turn removes any frequency dependence.

Figure 2 gives a comparison of displacement fields calculated by our infinite series formulation, i.e., inversion of equation (4), and by the numerical evaluation of two analytic closed form solutions. The upper pair of synthetics show the whole-space results, while the lower pair show the results for a source located at the center of the solid sphere in a whole-space. The formulation for the wave field outside of the solid sphere due to a centered explosion is given in Appendix B. The solutions, both closed and series, are calculated in the frequency domain and then transformed to the time domain, so that each pair of time histories shows almost identical precursor artifacts, which are caused by the numerical transforms. The agreement within pairs is excellent.

TABLE 1
MODEL

α (km/sec)	β (km/sec)	ρ (g/cm^3)	Radius (km)
1.80	0.41	1.84	0.5
4.55	2.57	2.45	∞

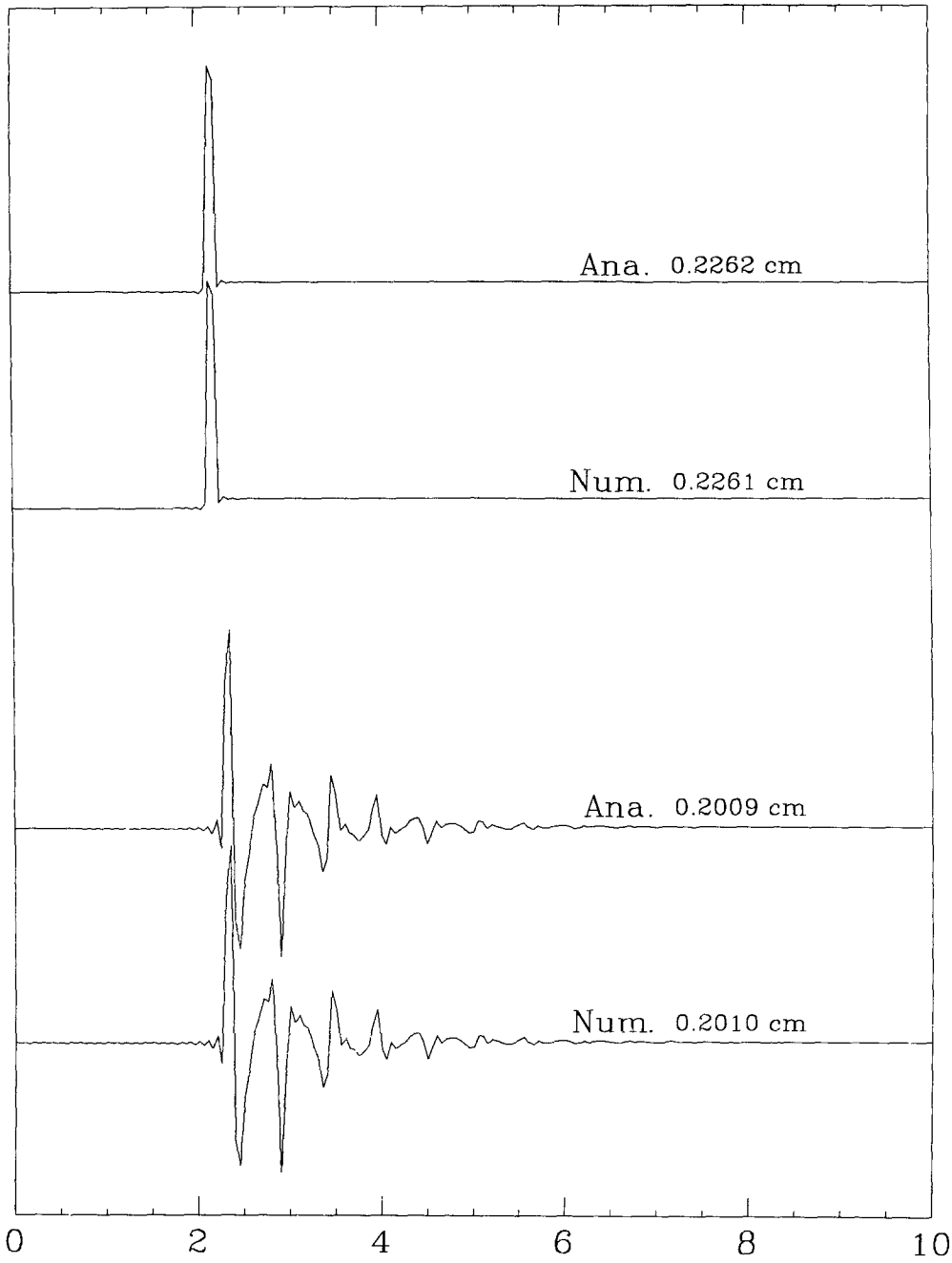

FIG. 2. Comparisons of numerical results with two known analytical solutions. The upper is for the wave fields of whole space, while the lower is for the wave fields from a centered source in an embedded sphere. "Num." denotes numerical and "Ana." denotes analytic.

In the following figures, we will refer to P- and S-wave arrivals as radial and azimuthal. These are $u_P{}^r$, $u_P{}^\delta$, $u_S{}^r$, and $u_S{}^\delta$, respectively, in the notation of the previous section. The P waves are the contribution to the displacement field from the P potential, begin at the P-wave arrival time, and physically corre-

spond to P or compressional waves arriving at the receiver that have undergone multiple reflections and conversions between P and S in the spherical source region. An analogous statement applies to the S waves with P replaced by S and compressional by shear. At a range, r, of 10 km for the standard model, the near-field P arrival $u_P{}^{\delta}$, which is the displacement component perpendicular to the propagation direction, and the near-field S arrival $u_S{}^{r}$, which is the component in the radial or propagation direction, are about 10% of the far-field arrivals $u_P{}^{r}$ and $u_S{}^{\delta}$. For a dynamic point source, one would expect far-field displacements to fall off as $1/r$ and the near-field to attenuate as $1/r^2$. This was investigated by generating wave fields at ranges from 5 to 40 km in 5-km intervals for the standard model. The waveform of each of these displacement components was found to be independent of range and by 10 km, the displacements fields indeed attenuated as predicted.

In most of the following examples, θ is set to 90°, i.e., the source and receiver are both in the horizontal plane. This was done to check our numerical algorithms for the transformations given in equation (8), which are used to obtain SV and SH displacements from the initial SV-only shear displacement field.

Figure 3 shows displacements at a receiver located at $(r, \theta, \phi) = (10, 90°, 90°)$, with the source at $(0.45, 90°, 180°)$. At these coordinates, the source and receiver position vectors are 90° to each other with respect to the sphere origin. We see that strong shear waves, as evidenced by the azimuthal component of S waves, are generated at receiver azimuths 90° from the symmetry axis of the source and the center of the sphere. Also the time difference between the two biggest arrivals in both the P and S waveforms is about 2.5 sec, which is the time needed for an S phase to travel through the sphere. This interval can be detected between many arrivals. Thus the bigger arrivals in the seismograms, except for direct P and S generated at the sphere boundary, can be interpreted as phases, which have traveled through the sphere at least once as S. The S-wave displacement is about a factor of 10 greater than the P-wave displacement. This is somewhat misleading, since, as we shall see in later examples, this is the azimuth of minimum P displacement and of maximum long-period S.

The change in displacement fields as a function of source asymmetry is displayed in Figure 4. The model and the geometry are the same as that used for Figure 3, except that the source radius, r_0, is varied from 0 to 0.45 km, the location in Figure 3, in 0.05 km increments. From this figure, we see that only P waves are generated when the source is at the center of the sphere, r_0 equal to 0. At this azimuth, as r_0 increases, the P-wave maximum amplitude is reduced by about a factor of 10, while the S-wave amplitude is increased to almost 50% greater than the P waves due to the centered source. The bottom traces, $r_0 = 0.45$ km, are the same as those in Figure 3 except on a common scale.

Figure 5 illustrates the effects on the wave fields as the velocity-density structure of the spherical source region is varied. The exterior medium properties are the same for all cases and are given in Table 1. The first row of traces are the same as those in Figure 3. For the bottom row, the sphere and surrounding space have identical properties and thus these traces are the results for an explosion in a whole-space. The source-receiver geometry is the same as Figure 3. We see that the greater the elastic contrast between the spherical source region and exterior medium, the greater the S waves generated. This is evidenced by the relative excitation between P and S on any given row. In making amplitude comparisons between differing source media in the

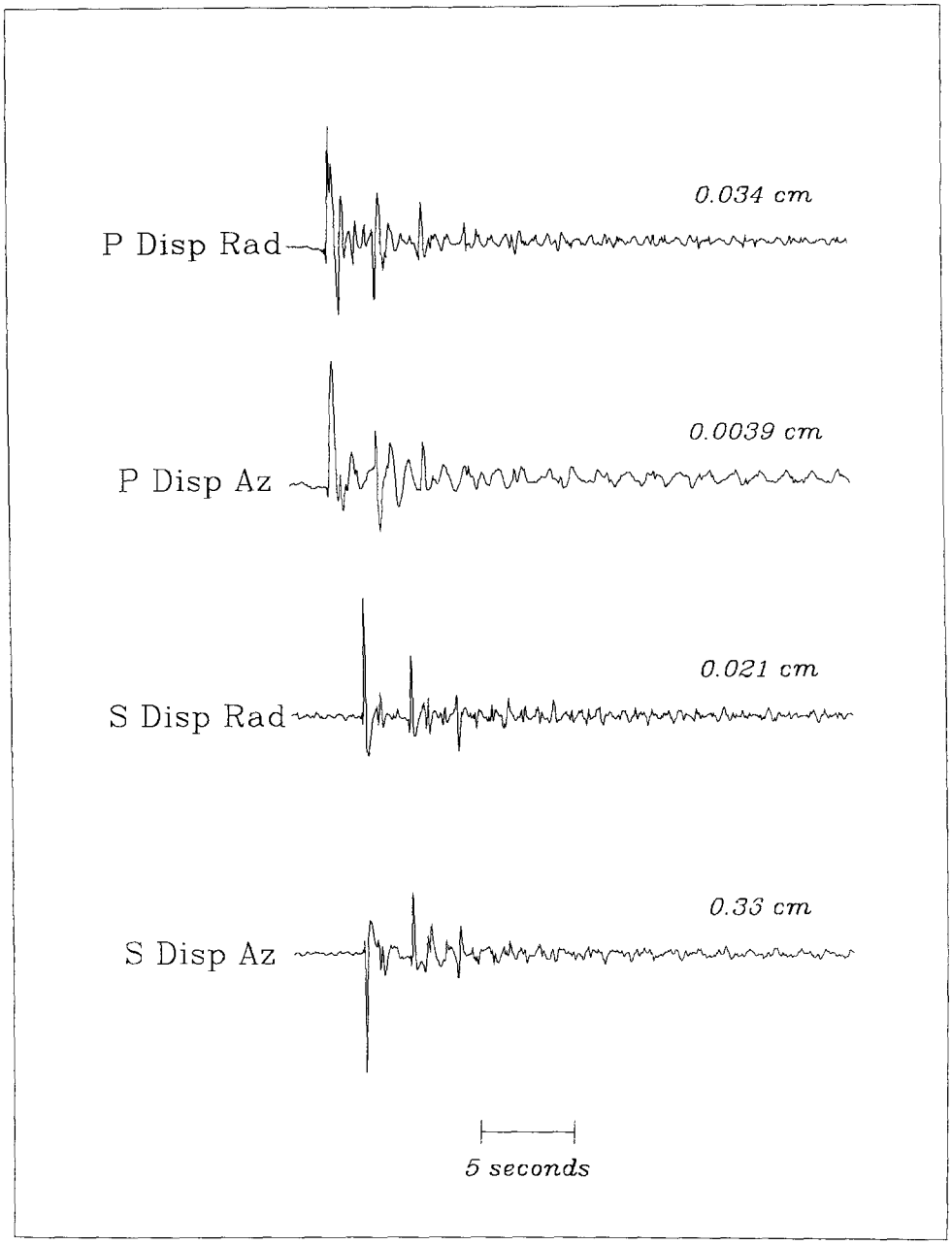

FIG. 3. An example of wave fields from an off-centered source in an embedded sphere with a radium of 0.5 km. "P" is for the P waves, and "S" is for the S waves. "Rad" is for the $\mathbf{e}_r$ component, and "Az" is for the $\mathbf{e}_\phi$ component. The numbers are the peak amplitudes.

figure, one must remember that the moment increases as one moves down the row with increasing velocities and density while $\Psi(\infty)$ remains unchanged.

Figure 6 shows the wave field variations as the angle, δ, between the source and receiver position vectors changes. When $\delta = 0$, the source, the receiver, and the center of the sphere are in a line. At this angle, no P or S δ components are generated. The near-field S r components are P-to-S conversions at the bound-

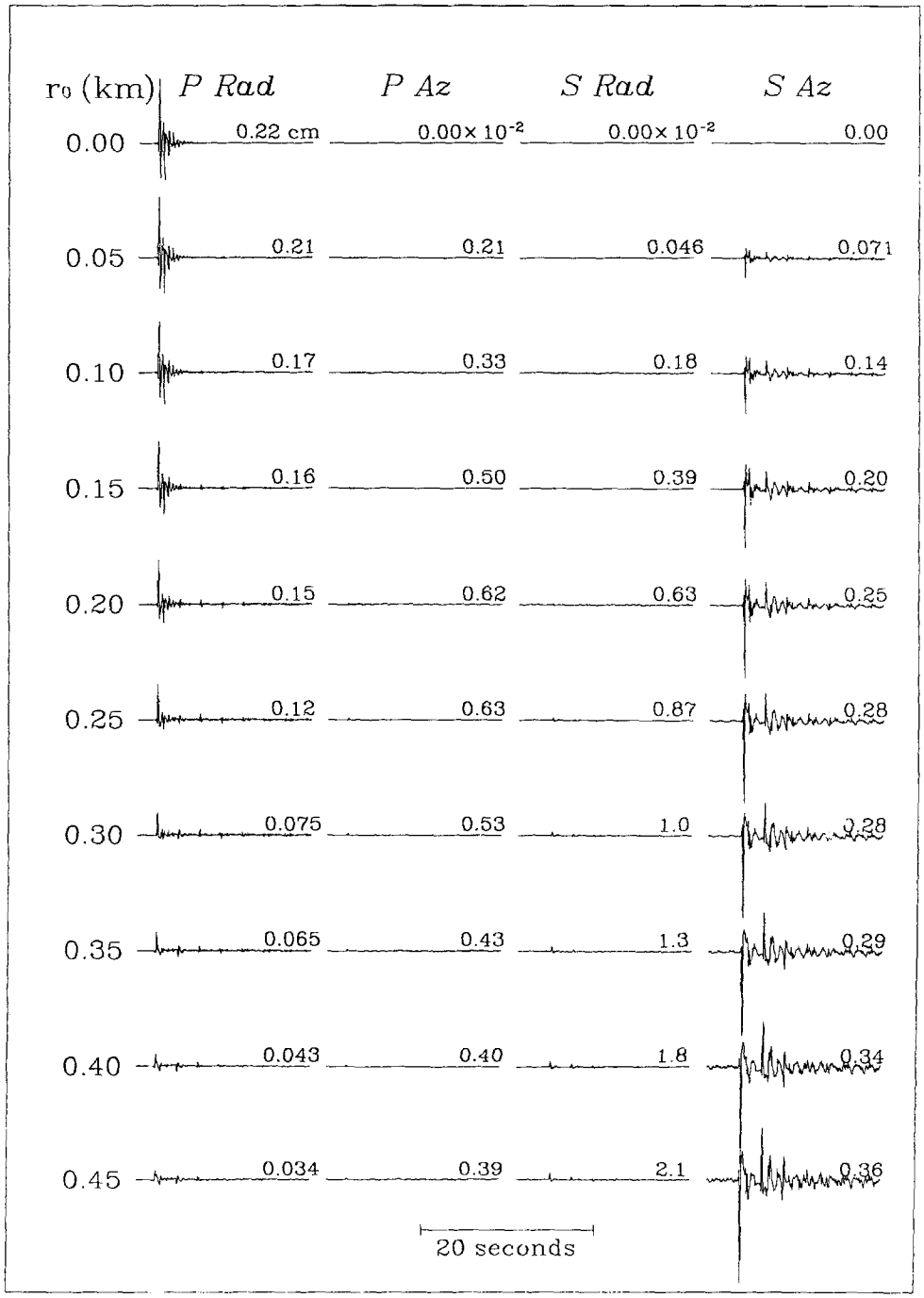

FIG. 4. Wave fields for different source distances to the center of the embedded sphere with a radium of 0.5 km. The 10^{-2} on the second and third traces of the first line, apply to all the traces in the second and third columns. r_0 is the distance from the source to the center. The vertical scale is same for all seismograms.

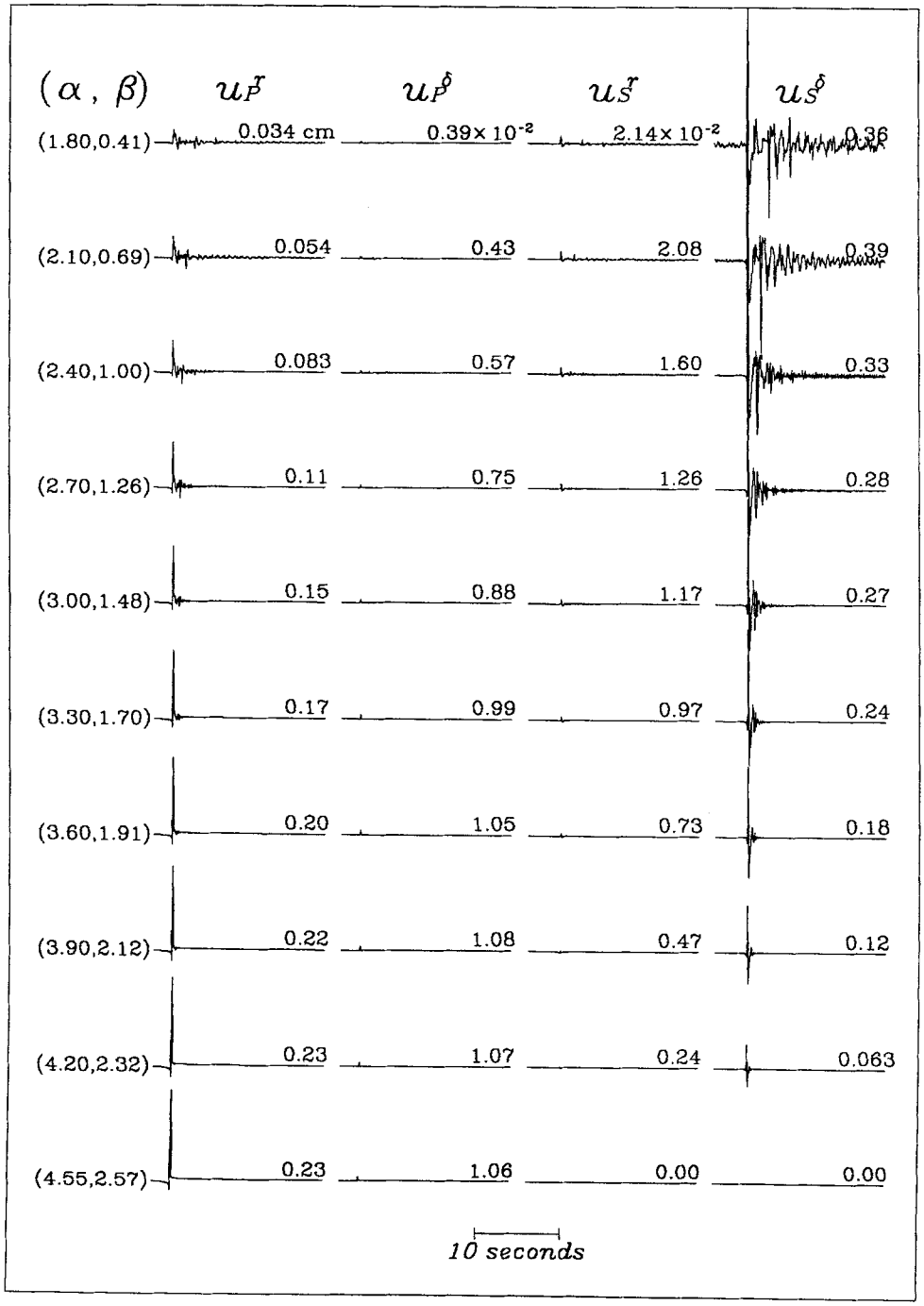

FIG. 5. Wave fields for different materials in the embedded sphere. α is compressional velocity, and β is shear velocity. Nafe's velocity-density relation is assumed for the shear velocity and density ρ.

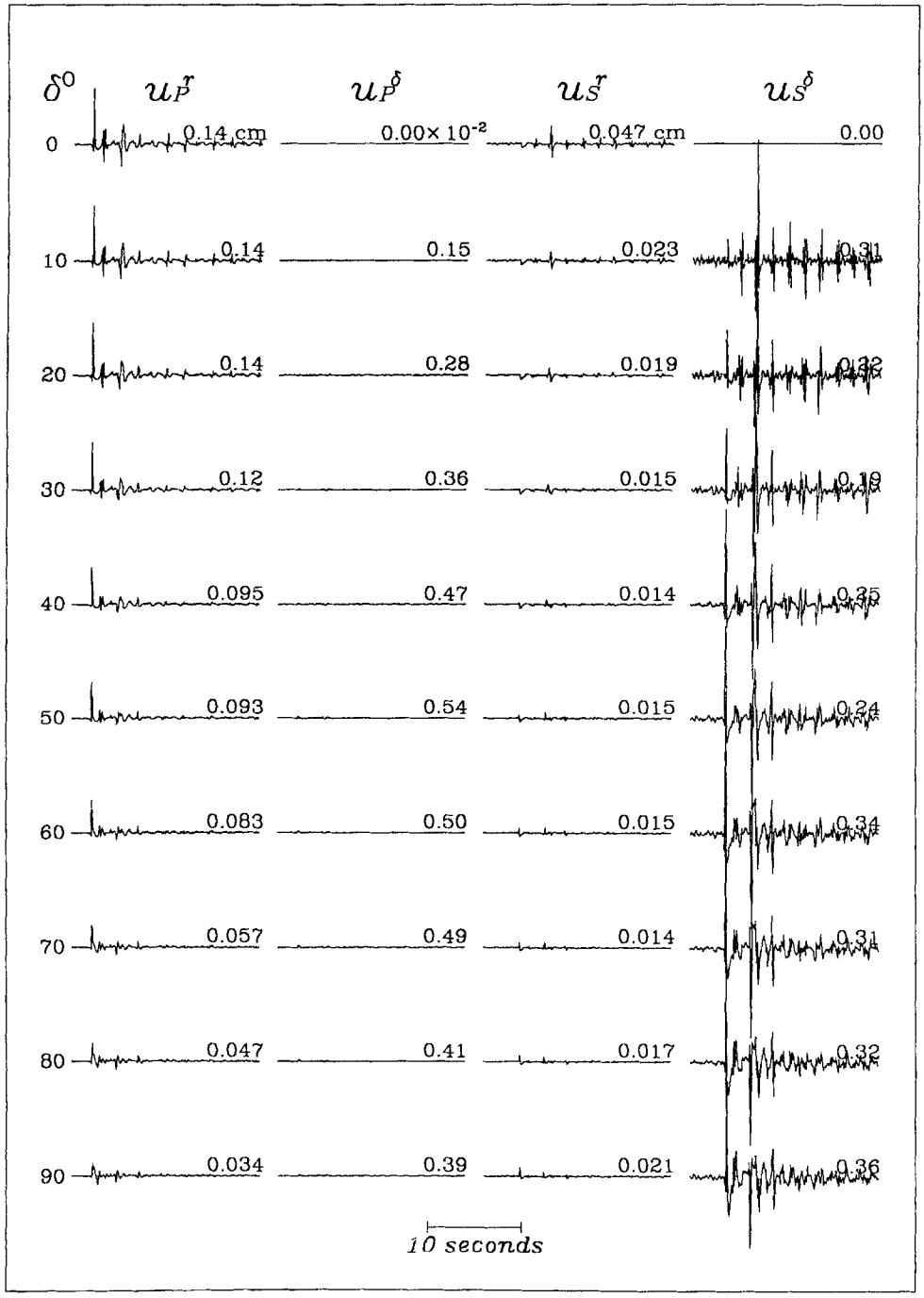

FIG. 6. Wave fields as a function of δ for the standard model. δ ranges from 0 to 90°.

ary that are focused back on the axis. The elastic sphere acts as a contact lens magnifying the the wave fields, like the Earth does at the antipode of an earthquake (Rial and Cormier, 1980). When δ increases, the P amplitude decreases, and S amplitude increases. The bottom traces are again those of

Figure 3. Comparing the bottom row with the top row and then with the top row of Figure 4, we see that the maximum S-wave amplitude is almost three times the maximum P-wave amplitude for this the maximum degree of asymmetry investigated and is more than 50% greater than the P-wave amplitude for the center explosion. Thus from Figures 4, 5, and 6, we see that the degree of asymmetry of the source region and the contrast between the media determine the intensity of the S-wave fields.

In Figure 7, we show the results for different sizes of the elastic sphere. The source radius is kept at the same fraction of the spheres's radius as in previous cases, i.e., r_0 is $0.9a$. The fourth row in the figure is the same as the last row in Figure 6 since the radii and source-receiver angles are the same, i.e., 0.5 km and 90°. Most of the observed effects can be explained by noting that increasing the radius under these conditions is similar to decreasing the velocity. Thus, we expect time differences between arrivals to increase and a decrease in frequency content as the radius increases.

Figure 8 displays the radial components of the P waves on the symmetry axis for different source radii with $\delta = 0$, i.e., source and receiver on the same side of sphere center and 180°, i.e., opposite sides. The distance used is 10 km from the source, while in previous figures the receiver was 10 km from the sphere center. If the source is located at the center of the solid sphere, the wave fields for $\delta = 0$, and 180° are of course identical. The numerical evaluation of the analytical solution was shown in Figure 2. As the source is moved toward the boundary of the sphere, the early arrivals separate and diminish in amplitude for $\delta = 0$. For $\delta = 180°$, they converge and grow in amplitude as the source passes through an effective focus in the sphere and then decrease in amplitude as the source is moved closer to the boundary.

In Figure 9, we keep the dimensions and source-receiver angles the same as Figure 8 but vary the sphere elastic properties using the same relationship between velocities and densities as before. The source radius is 0.45. The first row is the radial P wave field for velocities and density, which are the same as the previous figure. They can be considered an additional row to the previous figure with the source radius increased from 0.4 to 0.45 km. All traces on this figure are on a common scale in order to demonstrate the increase in amplitude of the early arrivals at $\delta = 0°$ and the reduction in amplitude of the later arriving S coupled internal reflections at both receiver positions as the velocities and density of the sphere are increased to that of the whole-space. The whole-space result is only slightly larger than the $\delta = 0°$ trace on the bottom and of course smaller than the $\delta = 180°$ bottom trace. The effect of decreasing the impedance contrast and of reducing the travel time for reflections in the sphere reduces the partitioning of direct P into later arrivals. The increase in moment while keeping $\Psi(\infty)$ constant as we go down the rows seems to have only a minor effect on the direct P amplitude. It is notable that the largest amplitude of direct P is in the middle rows where the elastic contrast is intermediate and in the receiver direction where the path is longest in the sphere, i.e., $\delta = 180°$. This is due to the source being near the focus, which changes position relative to source point as we change velocities. This is similar to the previous figure where we moved the source relative to the fixed focus.

With the exception of Figure 6, we have investigated the time histories at either the long-period maxima for the S waves, i.e., $\delta = 90°$ or at the P-wave maxima, i.e., $\delta = 0$ or 180°. Even in Figure 6, δ ranged only from 0 to 90°. In the

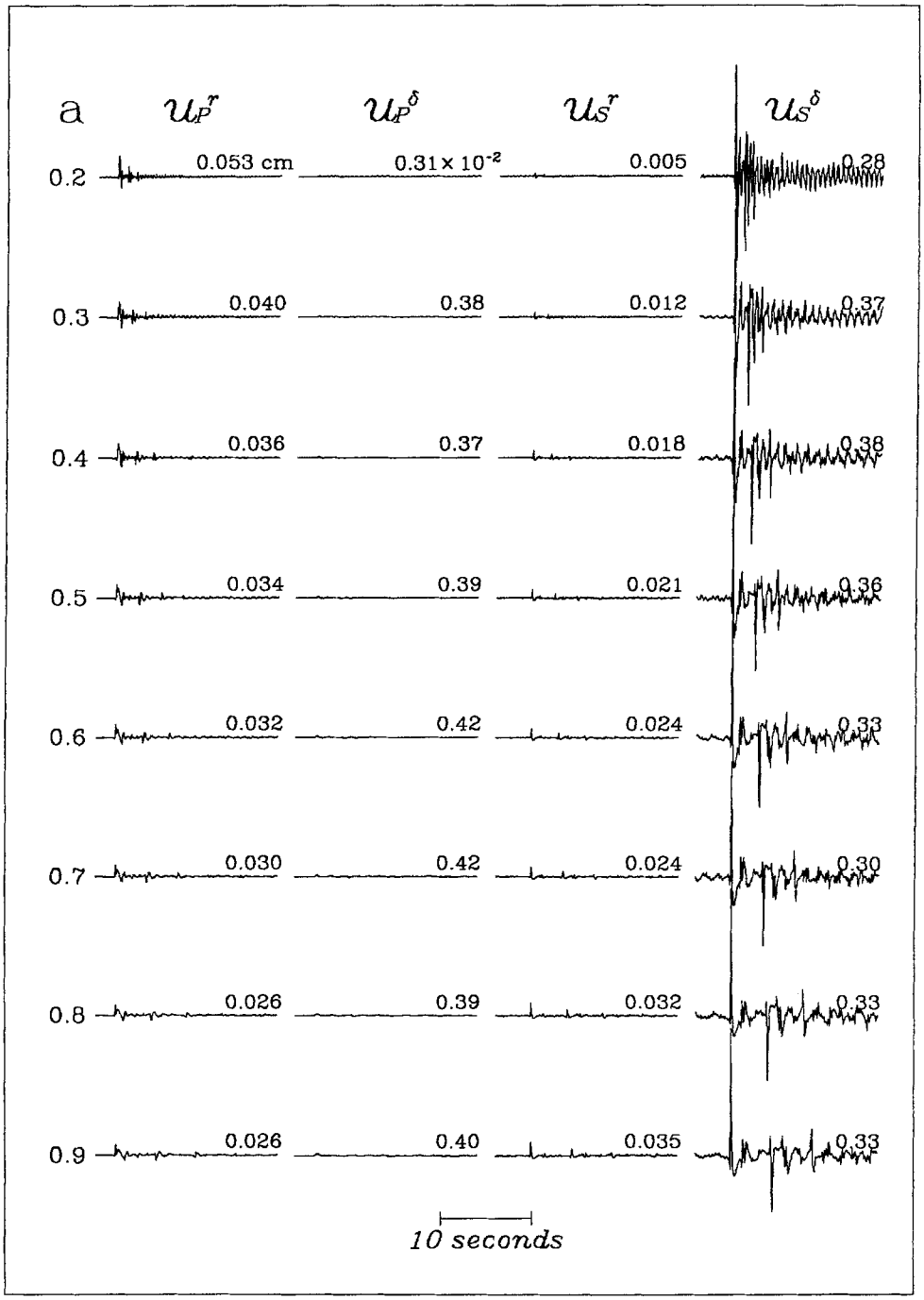

FIG. 7. Wave fields for different radii, 0.2 to 0.9 km, of the embedded sphere.

next three figures, we show the radiation pattern for P and S at periods of 1 and 20 sec as a function of source radius, elastic parameters, and radius of the sphere. The periods were chosen for their obvious significance to seismic magnitudes. The asymmetry of the source region is seen to have significant effects on

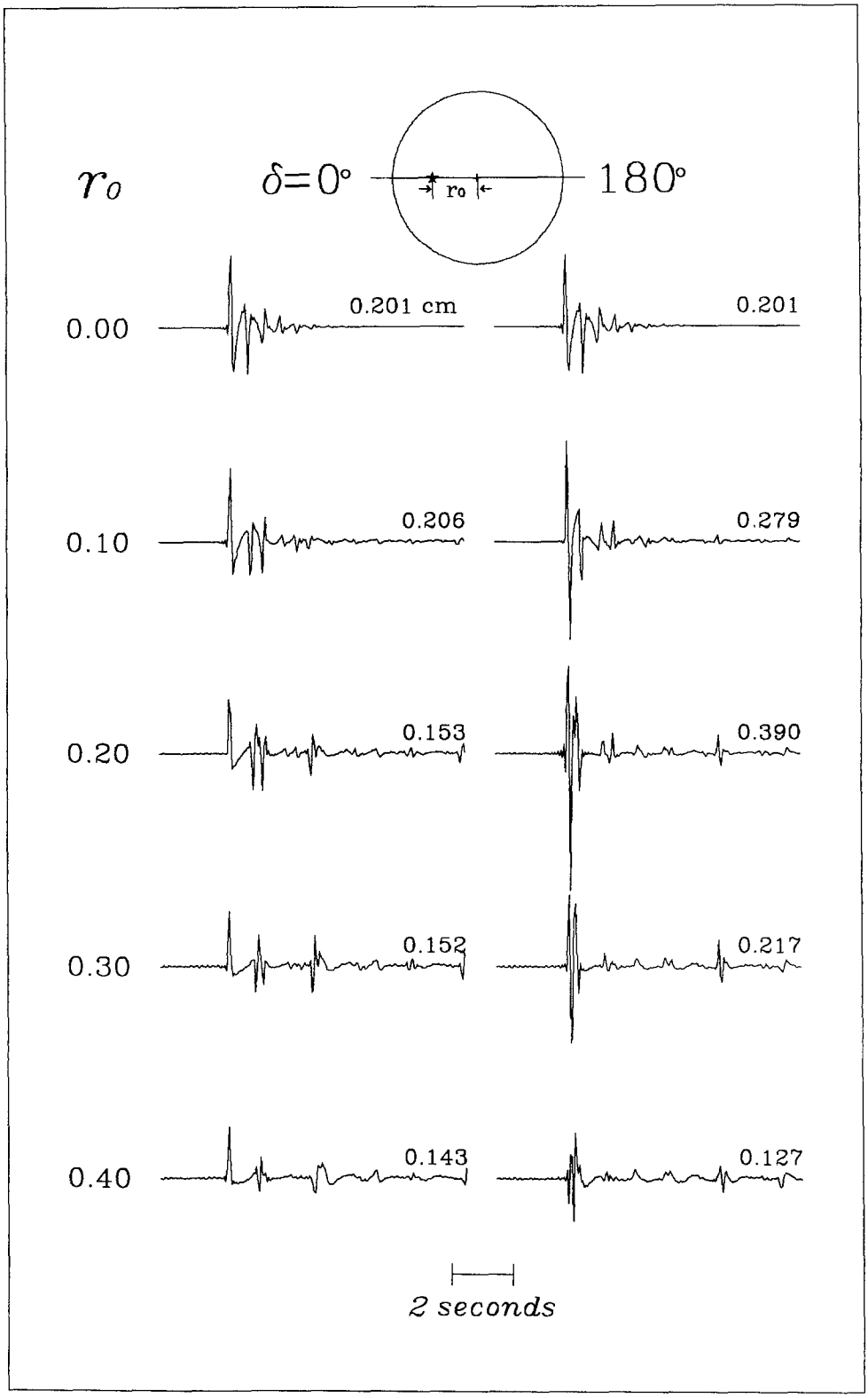

FIG. 8. Radial components of P waves at $\delta = 0$ and 180° for the different source locations. In the drawing of the sphere at the *top*, the star indicates the source.

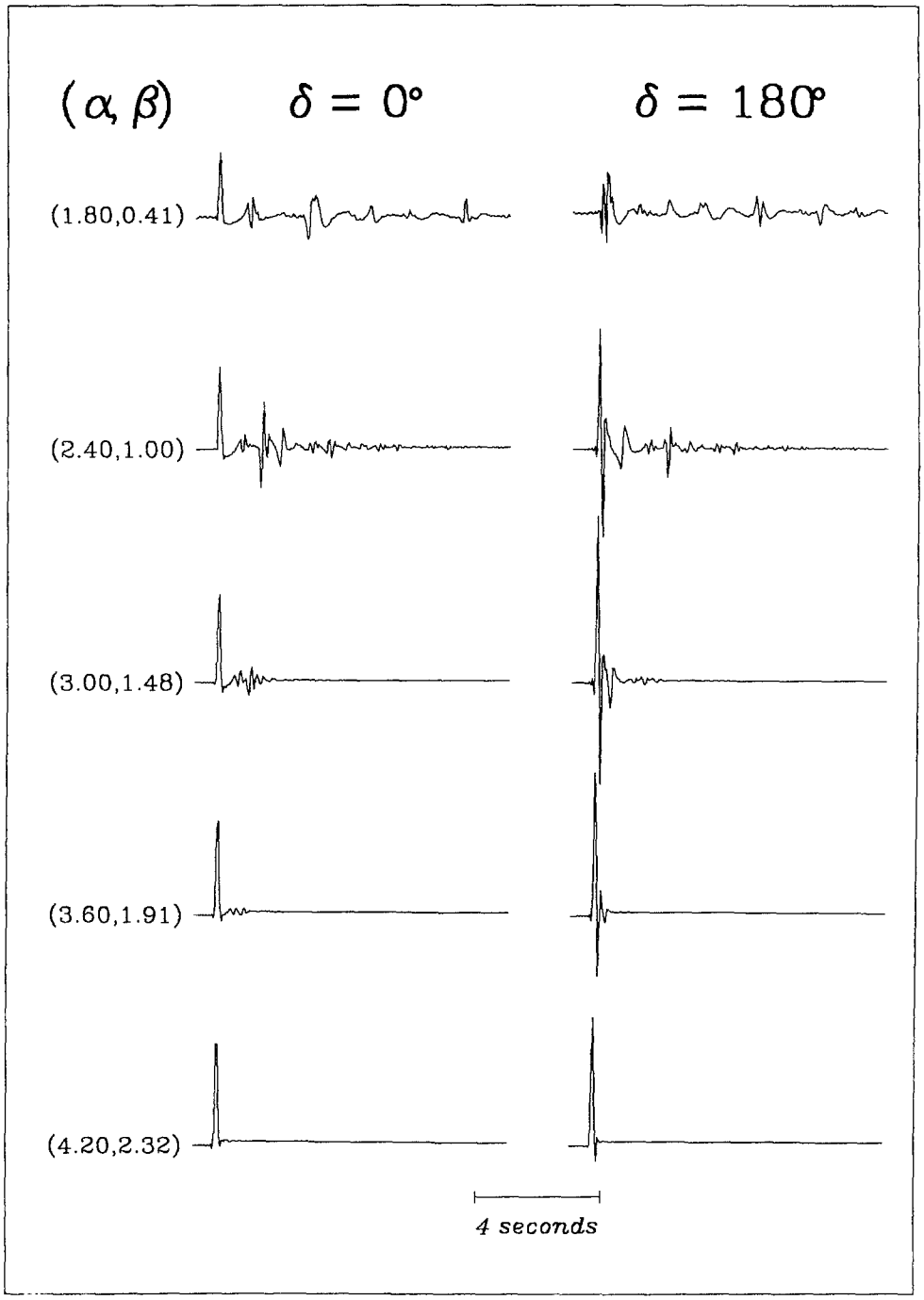

FIG. 9. Radial components of P waves at $\delta = 0$ and 180° for different P and S velocities and density in the sphere.

short-period radiation patterns, but to have only minor effects on the long period.

Figures 10, 11, and 12 show radiation patterns for different configurations. "P" and "S" in these figures denote the radial component of P waves and the δ

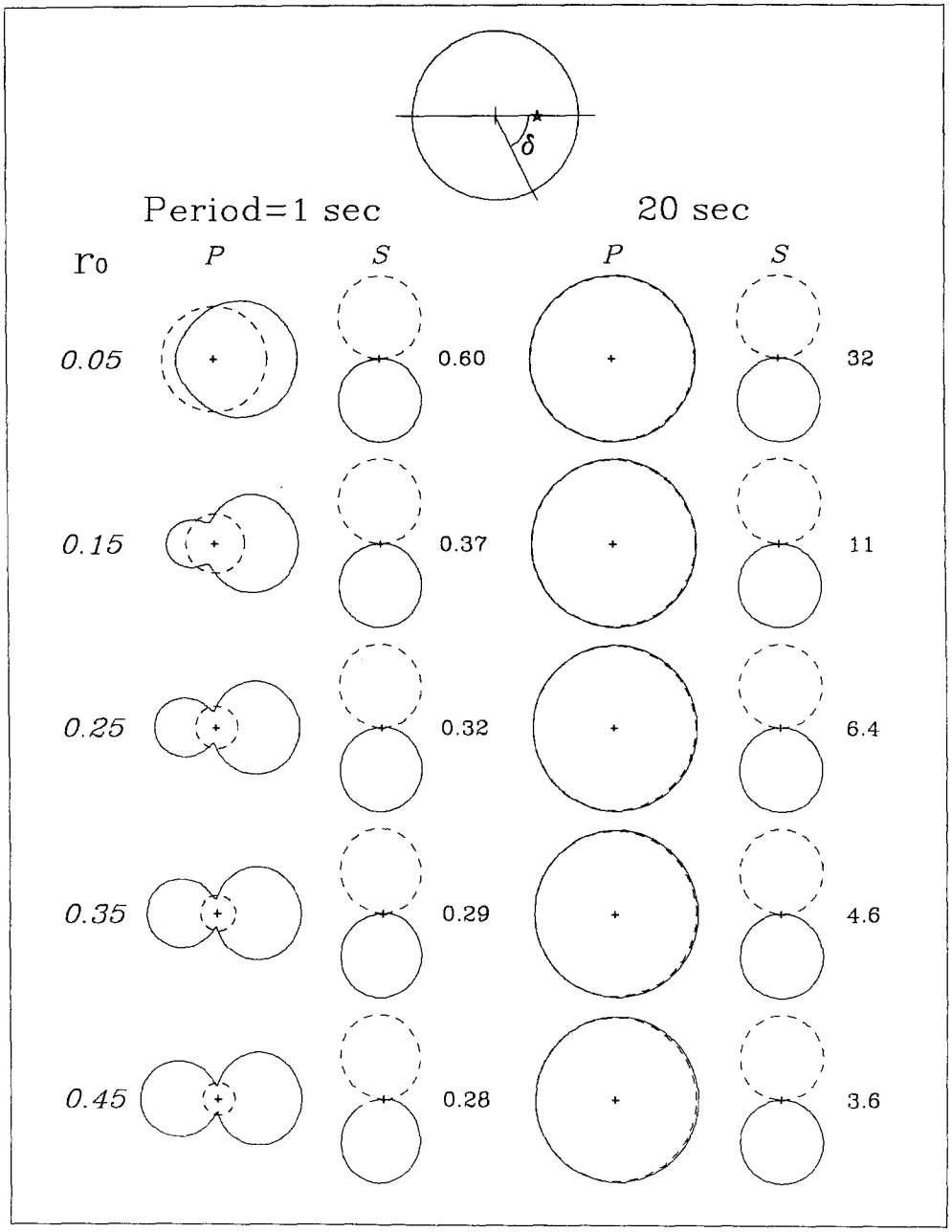

FIG. 10. Spectral radiation patterns at periods of 1 and 20 sec for different source locations. "P" is for the radial component of P waves, and "S" is for the δ component of S waves. On the drawing of the sphere at the *top*, the direction of δ is indicated. The star indicates the source. "+" is the center. Dash circles with the same centers as the P radiation patterns are the P-wave radiation patterns for a source located at the center. The numbers on the *right* of the S-wave radiation patterns are the multiplicative factors used to adjust the size of S-wave radiation patterns for comparison with the corresponding P-wave radiation patterns in the figure.

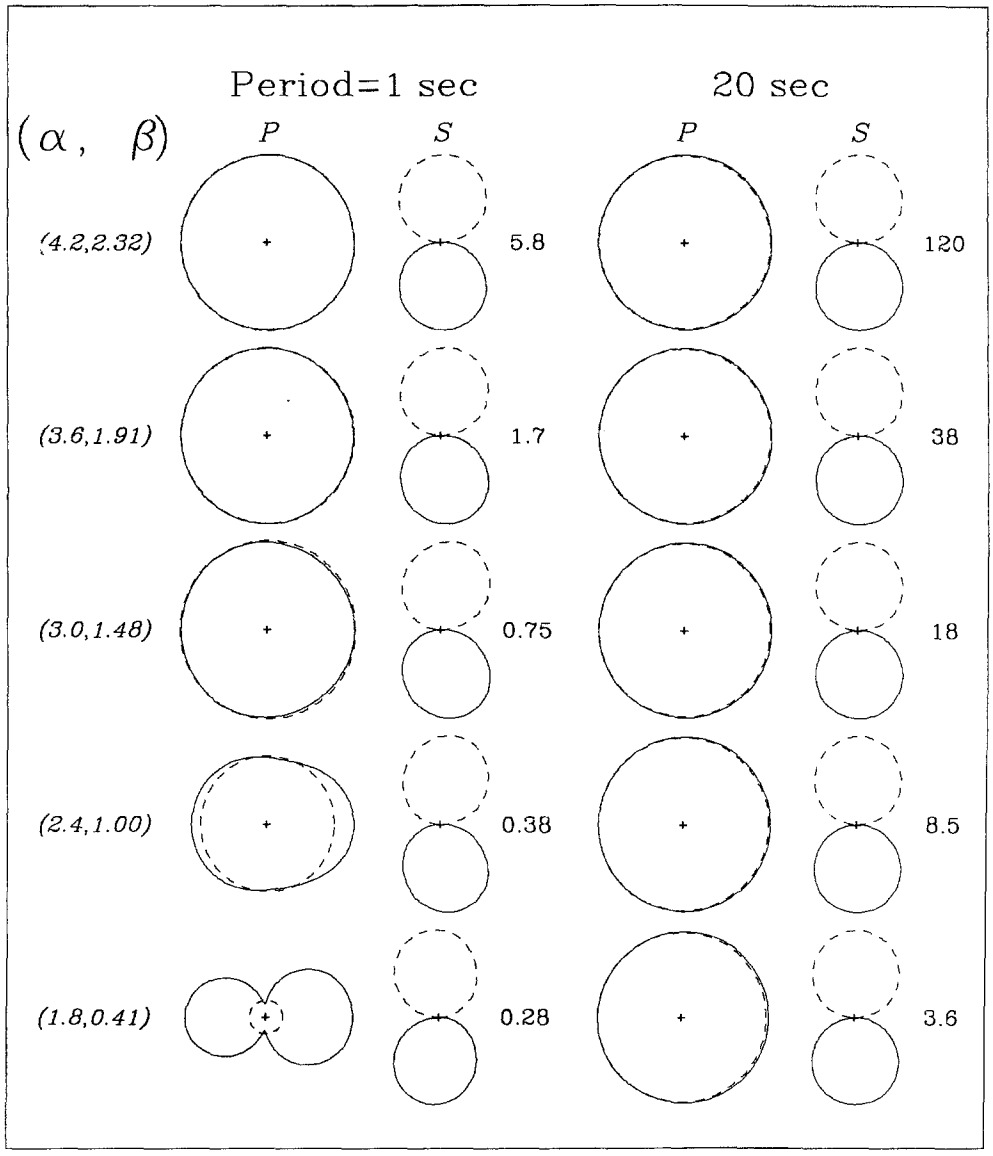

FIG. 11. Spectral radiation patterns for the different elastic media of the embedded sphere.

component of S waves, respectively. The distance used for these calculations is 1000 km to void the near-field contributions. The source is on the horizontal line for all these figures. The direction of δ is indicated on the diagram of the sphere at the top of Figure 10 with a star marking the source. The sphere center is shown as a "+" in all the radiation patterns. The dashed circles with the same centers as the P radiation patterns are the P-wave radiation pattern for the source located at the center for the particular model and demonstrate the amplitude effect due to source asymmetry. The dashed line part of the S-wave radiation pattern indicates negative amplitude compared to the solid line. In this case, positive indicates a clockwise displacement and negative is counter

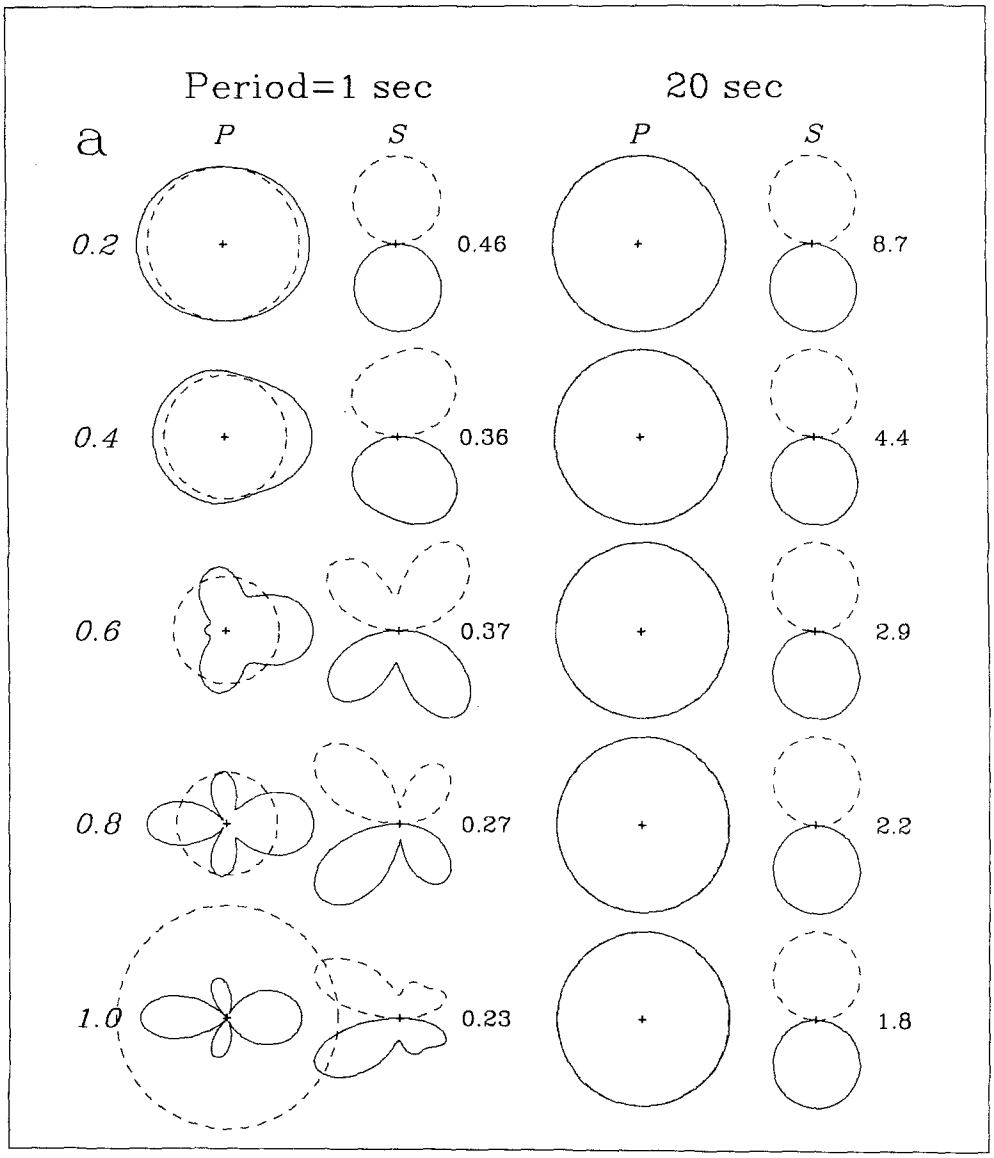

FIG. 12. Spectral radiation patterns for different radii of the elastic sphere.

clockwise. The number at the right-hand side of the S-wave radiation pattern is the multiplyer of the S-wave pattern used to plot on the figure; i.e., the larger the number the smaller the actual pattern compared to other S-wave patterns on the figure and the P-wave pattern next to it.

Figure 10, using the standard model, shows the radiation patterns for different source locations, r_0. Figure 12 uses the same elastic model but different radii of the solid sphere. In Figure 11, the sphere's elastic parameters are varied in the inverse order to Figure 9. Similar effects are seen in all three numerical experiments. As the source radius is increased, the elastic parameters of the sphere are decreased, or the sphere radius is increased, and the radiation patterns become more asymmetric. In other words, the P-wave radiation be-

comes less spherical and the 20-sec S-wave pattern, which is essentially the radiation pattern for a point force pointed away from the source, becomes larger. From these figures, we also see that the intensity of the P waves radiated by an off-center explosion is greater than that by the corresponding center explosion with the same $\Psi(\infty)$ except in Figure 12, where, increasing the source and sphere radius beyond the dimensions of the standard model, the opposite is true. Also by comparison within each row, we can see that S-wave generation is much smaller and that the P-wave fields are closer to the excitation of a center explosion for longer periods than for shorter periods.

An interesting feature is the shape of the radiation patterns at short periods. For the P wave in Figure 10 and 11, we see that the radiation pattern is similar to a dipole. The radiation patterns are reminiscent of those of far-field P and S waves scattered from localized inhomogeneities when plane P waves are incident (Aki and Richards, 1980, p. 732). This should not be surprising since in our case the incident wave is a spherical P wave interior to the scatterer. In comparing the Aki and Richards figure with ours, one must remember that our P-wave radiation patterns include the transmitted spherical wave perturbed by the scattering or asymmetric contribution, where theirs is only the scattered wave.

Another interesting feature in all three figures is that the maximum long-period 20-sec P-wave amplitudes are at least twice (≈ 1.8) as large as the corresponding maximum S-wave amplitudes for all cases calculated. This is in agreement with the empirical formula for explosions in axisymmetric cavities of Rial and Moran (1986). But because their sources were in the symmetry center of the cavity, the resulting S-wave radiation was more like a dipole than a point force at low frequencies.

In Figure 13, we investigate the error introduced if we estimate the moment by using a finite time length, which may include only the initial few pulses. The synthetics in Figure 13 are calculated for our standard velocity and density model keeping only $1/r$ terms, i.e., the far-field approximation. The distance used is 10 km from the center. The top trace is the response of a centered explosion; the lower one is the response of an off-center explosion. The source is 0.45 km from the center of the sphere and the angle, δ, between the source and receiver is 45°. From the long-period P-wave radiation patterns, we know that the angle is irrelevant as long as we are interested in moment. The moment is calculated from the area using the zero frequency spectra and corrected from "observed" to actual moment by equation (10). From the figure, the longer the time interval we use, the better the estimate we get. The first few pulses hold more than 80% of the moment in these two examples. Even though the first pulse holds about 90% of the moment, in a real situation it would be difficult to separate the effect of local reverberation. In this case, if we take a long enough window, the reverberations finally die down and we get a good estimate.

Figure 14 shows M_{obs}/M_0 as a function, equation (10), of the sphere compressional velocity, α_1, for different values of the whole-space compression velocities, α_2, assuming Nafe's velocity-density relation. For exterior velocities greater than those of the sphere, the "observed" moment M_{obs} is greater than the input M_0. And for velocities less, the opposite is true.

How and to what degree the energy for a given explosion is converted into seismic energy is beyond the expertise of the authors. We also do not know whether seismic moment or $\Psi(\infty)$ is the least affected by the physical properties

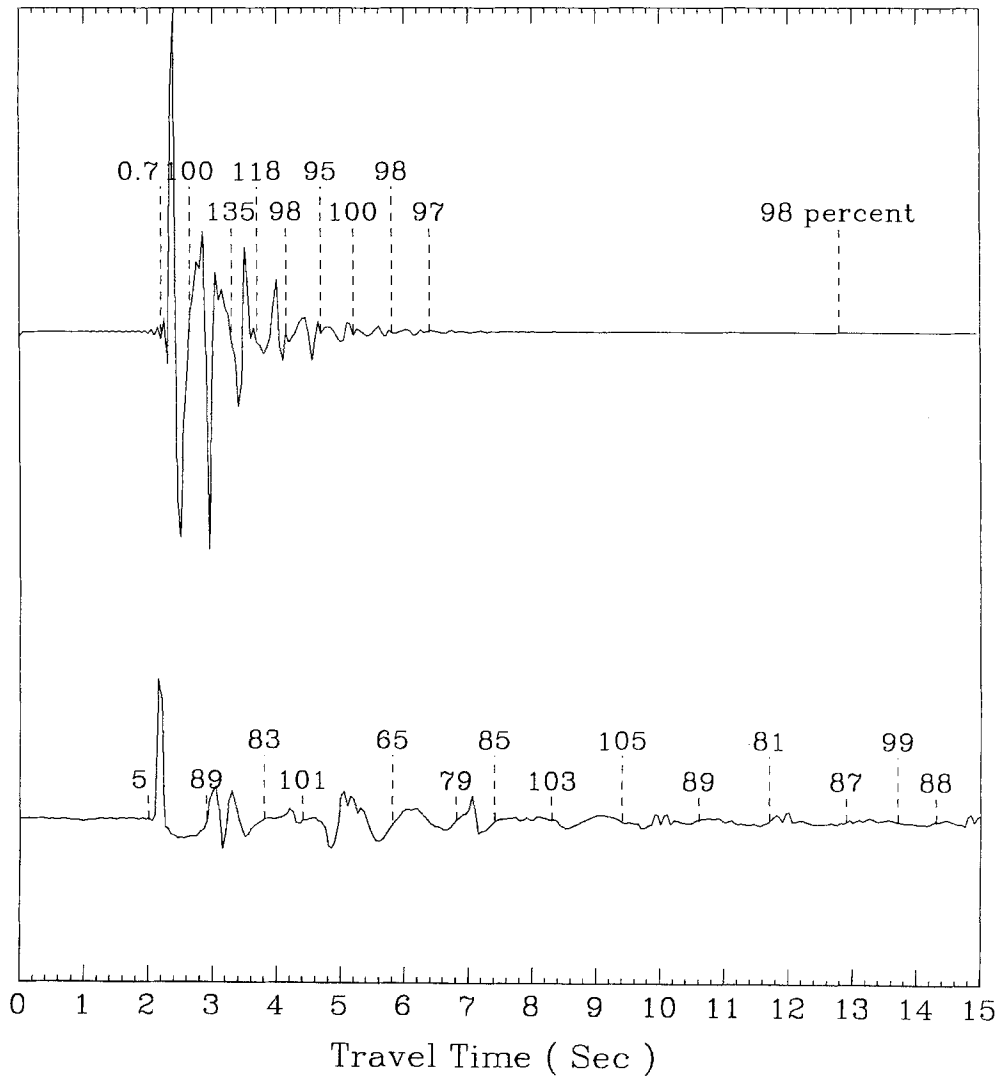

FIG. 13. Moment estimates as a function of record length. The numbers are the percentage of estimated moment to input moment obtained using the time length from the beginning to the dash line mark on the record below the number. The upper trace is the seismogram of a centered explosion. The lower one is the seismogram of an off-center explosion. Detailed parameters are given in the text.

of the shot point material and thus best characterizes an explosion of a given yield. For the numerical results given above, we have kept $\Psi(\infty)$ constant, and thus moment has varied as we changed the shot point medium. This was done for convenience and does not express an opinion on "seismic coupling."

CONCLUSIONS

In this study, we gave the analytical formulas for the wave fields from an off-center explosion in an embedded sphere. Numerical calculations were compared with the known analytic solutions. We also calculated P and S wave fields for different r_0, the source distance to the center (Fig. 4), for different

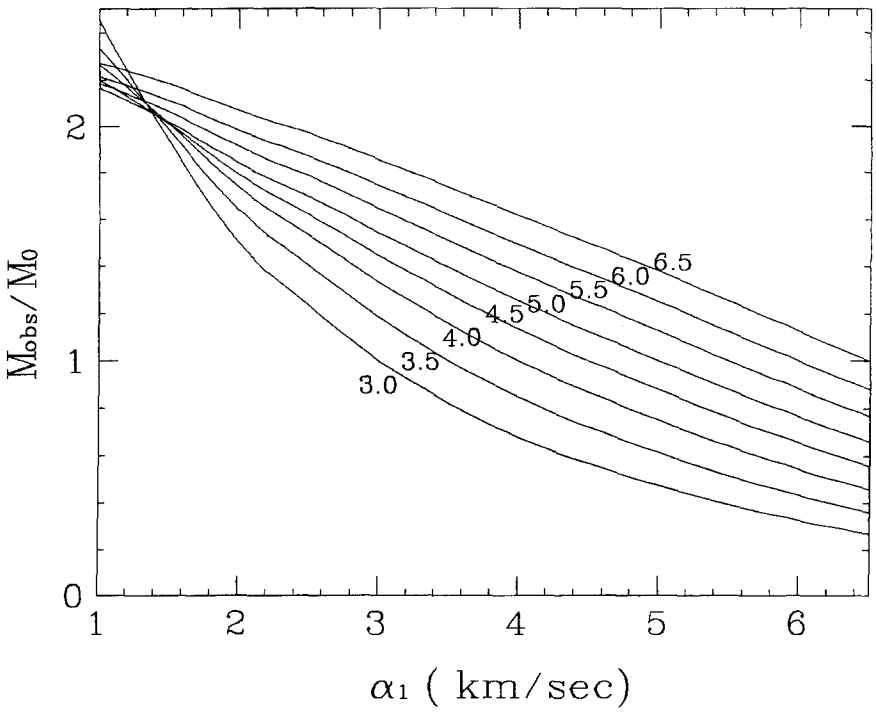

FIG. 14. Ratio of the "observed" moment to the input source moment, M_{obs}/M_0, as a function of the compressional velocities, α_1, of the embedded sphere for different whole-space velocities, α_2, assuming Nafe's velocity-density relation.

sphere materials (Fig. 5), for different azimuths, δ (Fig. 6), and for different sphere radii (Fig. 7). The degree of media contrast and the asymmetry of the source determined the size of *S*-wave generation. For the most extreme case investigated, we found that the maximum *S*-wave amplitude in the time domain is almost three times the maximum *P*-wave amplitude and is more than 50% greater than the *P*-wave amplitude for the center explosion. Before extrapolating these time-domain results to more realistic environments, one must remember that this is a very high-frequency source with a contribution to the far-field displacement, which is essentially flat in frequency.

In the frequency domain, the asymmetry of the source region has significant effects on the radiation patterns of short period but has only minor effects on that of long period. We also found that the maximum long-period *P*-wave amplitude was at least a factor of 2 greater than the *S*-wave maximum amplitude for our models. We also investigated the amount of moment error caused by using a finite time window. With care one can obtain meaningful estimates using only a short duration that contains relatively few pulses. Since the moment relation, which is obtained in the limit of zero frequency, is independent of the source location in the sphere and does not involve the geometry or dimensions of the sphere, we infer that it probably holds for embedded homogeneous source regions of any shape.

The long-period *SH*-wave radiation, which would be generated if the symmetry axis is in the horizontal, has a dipole radiation pattern. This is not the quadrupole radiation pattern proposed for known underground test sites.

ACKNOWLEDGMENTS

This research was supported by the Defense Advanced Research Projects Agency (DOD), Nuclear Monitoring Research Office, and was monitored by Air Force Geophysics Laboratory under Contract F19628-89-K-0028. Contribution No. 4993, Division of Geological and Planetary Sciences, California Institute of Technology, Pasadena, California.

REFERENCES

Aki, K. and P. G. Richards (1980). *Quantitative Seismology: Theory and Methods*, W. H. Freeman, San Francisco.

Aki, K. and Y. B. Tsai (1972). Mechanism of Love-wave excitation by explosive sources, *J. Geophys. Res.* **77**, 1452–1475.

Ben Menahem, A. and A. G. Sena (1990). The elastodynamic Green's tensor in an anisotropic half-space, *Geophys. J. Int.* **102**, 421–444.

Ben-Menahem, A. and S. J. Singh (1981). *Seismic Waves and Sources*, Springer-Verlag, New York.

Dubrovskiy, V. A. and V. S. Morochnik (1989). Nonstationary scattering of elastic waves by spherical inclusion, *Izvestiya, Earth Physics* **25**, 679–686.

Glenn, L. A., A. J. C. Ladd, B. Moran, and K. A. Wilson (1985). Elastic radiation from explosively-loaded ellipsoidal cavities in an unbounded medium, *Geophys. J. R. Astr. Soc.* **86**, 231–242.

Glenn, L. A., B. Moran, A. J. C. Ladd, K. A. Wilson, and J. A. Rial (1986). Elastic radiation from explosively-loaded axisymmetric cavities, *Geophys. J. R. Astr. Soc.* **86**, 119–136.

Harkrider, D. G., J. L. Stevens, and C. B. Archambeau (1992). Theoretical Rayleigh and Love waves from an explosion in prestressed source regions (submitted for publication).

Ludwig, W. J., J. E. Nafe, and C. L. Drake (1970). Seismic refraction, in *The Sea*, Vol. 4, Part I, A. E. Maxwell (Editor), Wiley, New York, 53–84.

Mandal, B. and M. N. Toksöz (1990). Computation of complete waveforms in general anisotropic media: results from an explosion source in an anisotropic medium, *Geophys. J. Int.* **103**, 33–45.

Pao, Y.-H. (1978). Betti's identity and transition matrix for elastic waves, *J. Acoust. Soc. Am.* **64**, 302–310.

Pao, Y. H. and C. C. Mow (1973). *Diffraction of Elastic Waves and Dynamic Stress Concentrations*, Crane, Russak and Co., New York.

Press, F. and C. B. Archambeau (1962). Release of tectonic strain by underground nuclear explosions. *J. Geophys. Res.* **67**, 337–343.

Rial, J. A. and V. F. Cormier (1980). Seismic waves at the epicenter's antipode, *J. Geophys. Res.* **85**, 2661–2668.

Rial, J. A. and B. Moran (1986). Radiation patterns for explosively-loaded axisymmetric cavities in an elastic medium: analytic approximations and numerical results, *Geophys. J. R. Astr. Soc.* **86**, 855–862.

Thompson, W. Jr. (1973). Acoustic radiation from a spherical source embedded eccentrically within a fluid sphere, *J. Acoust. Soc. Am.* **54**, 1694–1707.

Varatharajulu, V. and Y.-H. Pao (1976). Scattering matrix for elastic waves. I. Theory, *J. Acoust. Soc. Am.* **60**, 556–566.

Waterman, P. C. (1969). New formulation of acoustic scattering, *J. Acoust. Soc. Am.* **45**, 1417–1429.

Waterman, P. C. (1976). Matrix theory of elastic waves scattering, *J. Acoust. Soc. Am.* **60**, 567–580.

Zhao, L.-S., D. V. Helmberger, and D. G. Harkrider (1991). Shear-velocity structure of the crust and upper mantle beneath the Tibetan Plateau and southeastern China, *Geophys. J. Int.* **105**, 713–730.

APPENDIX A

For inclusion of this and rotated versions of this source into a vertically inhomogeneous half-space, it is convenient to express the source in terms of *P*- and *S*-wave potentials using the Helmholtz resolution,

$$\mathbf{u} = \nabla\Phi + \nabla \times \Psi, \tag{A1}$$

where Φ is the P-wave potential and Ψ is the S-wave potential. For the external medium, the P- and S-wave potentials can be expressed as

$$\Phi = \frac{1}{k_\alpha} \sum_{l=0}^{l=\infty} (2l + 1) d_l h_l^{(2)}(k_\alpha r) P_l(\cos \delta), \tag{A2}$$

$$\Psi = -\frac{1}{k_\beta} \sum_{l=0}^{l=\infty} (2l + 1) c_l h_l^{(2)}(k_\beta r) \frac{d}{d\delta} P_l(\cos \delta)\mathbf{e}. \tag{A3}$$

For the translated coordinate system with the source located at (r_0, θ_0, ϕ_0), Figure 1, we use the addition theorem for zonal harmonics

$$P_l(\cos \delta) = \sum_{m=0}^{l} \epsilon_m \frac{(l - m)!}{(l + m)!} P_l^m(\cos \theta) P_l^m(\cos \theta_0) \cdot(\cos m \phi \cos m \phi_0 + \sin m \phi \sin m\phi_0). \tag{A4}$$

Substituting (A4) into equation (A2), we obtain equation (A5):

$$\Phi = -\frac{1}{k_\alpha^2} \sum_{n=0}^{n=\infty} \sum_{m=0}^{m=n} [A_{nm} \cos m\phi + B_{nm} \sin m\phi] P_n^m(\cos \theta) h_n^{(2)}(k_\alpha r), \tag{A5}$$

where

$$A_{nm} = -(2n + 1) \frac{(n - m)!}{(n + m)!} k_\alpha d_n \epsilon_m P_n^m(\cos \theta_0) \cos m\phi_0, \tag{A6}$$

$$B_{nm} = -(2n + 1) \frac{(n - m)!}{(n + m)!} k_\alpha d_n \epsilon_m P_n^m(\cos \theta_0) \sin m\phi_0.$$

For the shear potential, we implicitly define ψ as

$$\Psi = \psi \mathbf{e}_\gamma,$$

and in the translated coordinates

$$\Psi = \psi^r \mathbf{e}_r + \psi^\theta \mathbf{e}_\theta + \psi^\phi \mathbf{e}_\phi$$

with

$$\psi^r = 0,$$

$$\psi^\theta = -\psi \sin \theta_0 \sin(\phi - \phi_0)/\sin \delta,$$

and

$$\psi^{\phi} = -\psi(\sin\theta_0\cos\theta\cos(\phi-\phi_0) - \cos\theta_0\sin\theta)/\sin\delta.$$

Defining

$$\boldsymbol{\phi}_n = \frac{d}{d\delta}P_n(\cos\delta)\mathbf{e}_\gamma$$

or

$$\boldsymbol{\phi}_n = -P_n'(\cos\delta)\mathbf{e}_{r_0}\times\mathbf{e}_r,$$

we obtain

$$\begin{aligned}
\phi_{n1} &= -P_n'(\cos\delta)(\sin\theta_0\sin\phi_0\cos\theta - \sin\theta\sin\phi\cos\theta_0),\\
\phi_{n2} &= -P_n'(\cos\delta)(\cos\theta_0\sin\theta\cos\phi - \sin\theta_0\cos\phi_0\cos\theta),\\
\phi_{n3} &= -P_n'(\cos\delta)\sin\theta_0\sin\theta\sin(\phi-\phi_0),
\end{aligned}$$

where

$$P_n'(\cos\delta) = \frac{dP_n(\cos\delta)}{d\cos\delta}.$$

Then,

$$\frac{\partial P_n(\cos\delta)}{\partial\phi_0} = P_n'(\cos\delta)\sin\theta\sin\theta_0\sin(\phi-\phi_0) = -\phi_{n3},$$

$$\phi_{n1} = \sin\phi_0\frac{\partial P_n(\cos\delta)}{\partial\theta_0} - \cot\theta_0\cos\phi_0\cdot\phi_{n3},$$

$$\phi_{n2} = -\cos\phi_0\frac{\partial P_n(\cos\delta)}{\partial\theta_0} - \cot\theta_0\sin\phi_0\cdot\phi_{n3}.$$

From these relations, it is not difficult to get equation (A7) in a manner similar to equation (A5):

$$\boldsymbol{\Psi}_j = -\frac{2}{k_\beta^{\,2}}\sum_{n=0}^{n=\infty}\sum_{m=0}^{m=n}\left[C_{nm}^{(j)}\cos m\phi + D_{nm}^{(j)}\sin m\phi\right]P_n^{\,m}(\cos\theta)h_n^{(2)}(k_\beta r), \quad \text{(A7)}$$

where Ψ_j ($j = 1, 2, 3$) are the Cartesian components of the S-wave potential Ψ, and

$$C_{nj}^{(1)}m = -\frac{k_\beta}{2}(2n+1)\frac{(n-m)!}{(n+m)!}\epsilon_m c_n\left[\frac{d}{d\theta_0}P_n^m(\cos\theta_0)\sin\phi_0\cos m\phi_0 - mP_n^m(\cos\theta_0)\cot\theta_0\cos\phi_0\sin m\phi_0\right],$$

$$D_{nm}^{(1)} = -\frac{k_\beta}{2}(2n+1)\frac{(n-m)!}{(n+m)!}\epsilon_m c_n\left[\frac{d}{d\theta_0}P_n^m(\cos\theta_0)\sin\phi_0\sin m\phi_0 + mP_n^m(\cos\theta_0)\cot\theta_0\cos\phi_0\cos m\phi_0\right],$$

$$C_{nm}^{(2)} = \frac{k_\beta}{2}(2n+1)\frac{(n-m)!}{(n+m)!}\epsilon_m c_n\left[\frac{d}{d\theta_0}P_n^m(\cos\theta_0)\cos\phi_0\cos m\phi_0 + mP_n^m(\cos\theta_0)\cot\theta_0\sin\phi_0\sin m\phi_0\right],$$

$$D_{nm}^{(2)} = \frac{k_\beta}{2}(2n+1)\frac{(n-m)!}{(n+m)!}\epsilon_m c_n\left[\frac{d}{d\theta_0}P_n^m(\cos\theta_0)\cos\phi_0\sin m\phi_0 - mP_n^m(\cos\theta_0)\cot\theta_0\sin\phi_0\cos m\phi_0\right],$$

$$C_{nm}^{(3)} = -\frac{k_\beta}{2}(2n+1)\frac{(n-m)!}{(n+m)!}\epsilon_m c_n P_n^m(\cos\theta_0)\sin m\phi_0,$$

$$D_{nm}^{(3)} = \frac{k_\beta}{2}(2n+1)\frac{(n-m)!}{(n+m)!}\epsilon_m c_n P_n^m(\cos\theta_0)\cos m\phi_0, \tag{A8}$$

where $\epsilon_m = 1$ if $m = 0$, $\epsilon_m = 2$ if $m \neq 0$. Ψ_3 is the SH-wave potential.

From the equations (A8), we see that SH waves will be generated if $C_{nm}^{(3)}$ and $D_{nm}^{(3)}$ are not 0 in Cartesian coordinate system. Harkrider *et al.* (1992) give a detailed derivation of the surface waves in layered media due to a transparent source expressed in the general form (A5) and (A7).

When the explosion source is on the z axis, as in equation (A3), there are only SV waves because of symmetry. As one moves the source off the z axis, the $C_{nm}^{(3)}$ and $D_{nm}^{(3)}$ are no longer zero and we have SH waves as one would expect.

APPENDIX B

In this appendix, we give the analytic solution for the source at the center of the cavity. From equation (1), we have

$$\mathbf{u}_1 = A\mathbf{L}_{0,0}^{-}(k_{\alpha_1}r) - b\mathbf{L}_{0,0}^{+}(k_{\alpha_1}r), \tag{B1}$$

$$\mathbf{u}_2 = d\mathbf{L}_{0,0}^{-}(k_{\alpha_2}r), \tag{B2}$$

where A is $ik_{\alpha 1}^2 g(\omega)A_0$. Other terms in (1) are 0. From the boundary condition at $r = a$, we have

$$\begin{pmatrix} b \\ d \end{pmatrix} = \frac{A}{\Delta}\begin{bmatrix} F_{0,3}^{-}(\xi_2) & -h_0^{(2)'}(\xi_2) \\ -\gamma F_{0,3}^{+}(\xi_1) & j_0'(\xi_1) \end{bmatrix}\begin{pmatrix} h_0^{(2)'}(\xi_1) \\ \gamma F_{0,3}^{-}(\xi_1) \end{pmatrix}, \tag{B3}$$

where $\xi_i = k_{\alpha_i} a$, $\gamma = \mu_1 k_{\alpha_1}/\mu_2 k_{\alpha_2}$, and

$$\Delta = F_{0,3}^{-}(\xi_2) j_0'(\xi_1) - \gamma h_0^{(2)'}(\xi_2) F_{0,3}^{+}(\xi_1).$$

According to the relations of Bessel functions, we have

$$\Delta = h_0^{(2)}(\xi_2) j_0(\xi_1)\left[\left(\cot\xi_1 - \frac{1}{\xi_1}\right)\left(i + \frac{1}{\xi_2}\right)\left(\frac{2}{\xi_2} - \frac{2\gamma}{\xi_1}\right)\right.$$
$$\left. - \frac{1}{2}\left(\frac{\alpha_2}{\beta_2}\right)^2\left(\cot\xi_1 - \frac{1}{\xi_1}\right) - \frac{1}{2}\left(\frac{\alpha_1}{\beta_1}\right)^2 \gamma\left(i + \frac{1}{\xi_2}\right)\right].$$

From equations (B2) and (B3), $\mathbf{u}_2$ can be written as

$$\mathbf{u}_2 = \frac{A_0}{2a^2\Delta} g(\omega) \frac{\mu_1 k_{\alpha_1}}{\mu_2 k_{\alpha_2}} \left(\frac{\alpha_1}{\beta_1}\right)^2 h_0^{(2)'}(k_{\alpha_2} r)\mathbf{e}_r. \tag{B4}$$

SEISMOLOGICAL LABORATORY
CALIFORNIA INSTITUTE OF TECHNOLOGY
PASADENA, CALIFORNIA 91125

Manuscript received 20 March 1991